

MODEL PREDICTIVE CONTROL OF AN ACTIVE MAGNETIC BEARING SUSPENDED FLYWHEEL ENERGY STORAGE SYSTEM

K.R. Uren*, G. van Schoor[†] and C.D. Aucamp*

* School of Electrical, Electronic and Computer Engineering, North-West University, Potchefstroom campus, Hoffman street, South Africa. E-mail: kenny.uren@nwu.ac.za, christiaan.aucamp@gmail.com

[†] Unit for Energy Systems, North-West University, Potchefstroom campus, Hoffman street, South Africa. E-mail: george.vanschoor@nwu.ac.za

Abstract: Flywheel Energy Storage (FES) is rapidly becoming an attractive enabling technology in power systems requiring energy storage. This is mainly due to the rapid advances made in Active Magnetic Bearing (AMB) technology. The use of AMBs in FES systems results in a drastic increase in their efficiency. Another key component of a flywheel system is the control strategy. In the past, decentralised control strategies implementing PID control, proved very effective and robust. In this paper, the performance of an advanced centralised control strategy namely, Model Predictive Control (MPC) is investigated. It is an optimal Multiple-Input and Multiple-Output (MIMO) control strategy that utilises a system model and an optimisation algorithm to determine the optimal control law. A first principle state space model is derived for the purpose of the MPC control strategy. The designed MPC controller is evaluated both in simulation and experimentally at a low operating speed as a proof of concept. The experimental and simulated results are compared by means of a sensitivity analysis. The controller showed good performance, however further improvements need to be made in order to sustain good performance and stability at higher speeds. In this paper advantages of incorporating a system model in a model-based strategy such as MPC are illustrated. MPC also allows for incorporating system and control constraints into the control methodology allowing for better efficiency and reliability capabilities.

Key words: state space model, model predictive control, flywheel energy storage system, active magnetic bearings

1. INTRODUCTION

Early applications of flywheels mainly centred around the smooth operation of machines. The type of flywheels used were purely mechanical, and some primitive versions only consisted of a stone wheel attached to an axle. The development of flywheel systems continued through the years, but rapidly intensified during the Industrial Revolution. However, it was not until the early 20th century, when flywheel rotor shapes and rotational stresses were thoroughly analysed in the work reported by Stodola [1]. In the 1970s, FES was proposed as a key technology for electric vehicles, spacecraft, Uninterruptible Power Supplies (UPSs) and even planetary rovers [2, 3]. During the 1980s, Active Magnetic Bearings (AMBs) and advances in motor-generator designs placed FES systems in a position to compete with chemical batteries in terms of energy density [4–6].

FES systems have a number of attributes that render them preferred technology for applications where energy storage is needed. Flywheel systems are made of environmentally friendly material as opposed to chemical batteries, and therefore have a lower environmental impact. It is a scalable technology and does not require periodic maintenance. Flywheels also allow repetitive deep discharge. The contact-less nature of magnetic bearings allows for higher energy efficiency, and no lubricants are necessary. The closed-loop control of magnetic bearings enables active vibration suppression and on-line control of

bearing stiffness. According to Schweitzer et.al. [7], the most effective and simplest control strategy for a coupled system such as a FES system is decentralised and conical mode control. Examples of these types of strategies are decentralised PID control, and Centre-Of-Gravity (COG) coordinate control. Modern control techniques that give promising results for controlling AMB systems are \mathcal{H}_∞ and μ -synthesis, in particular for flexible rotor systems [8–13]. Schweitzer et.al. [7] continues by stating that observer or state estimator based control such as Linear-Quadratic-Gaussian (LQG) control offers no appreciable advantage over decentralised control. In fact, observer based techniques can have destabilising effects due to uncertain dynamics in AMBs during rotation. In the case where the observer based control is designed for a rotating system, the controller may be very effective at the design speed, but may become unstable at other speeds due to non-conservative forces introduced by the controller. This is particularly the case for model based control techniques where the dynamics of the system change as the rotational speed changes. This raises the question whether an advanced model-based control technique such as MPC can be successfully implemented on a FES system.

MPC has a number of advantages. It is firstly capable of handling constraints explicitly. Secondly it treats multi-variable problems in a natural way and it incorporates a model-based design in the sense that it uses an explicit internal model to generate predictions of future plant behaviour. A number of studies were

previously conducted to evaluate the performance of MPC control strategies on magnetically suspended FES systems. Zhang et. al. [14] conducted a study where a FES system was proposed where the radial motion of the rotor was controlled by permanent magnet bearings, and the axial motion was controlled by AMBs that utilised an MPC strategy. This study was only implemented in simulation, but concluded that MPC yielded superior stability, sensitivity and robustness as compared to PID control. Another study conducted by Zhu et. al. [15] focused on the cross-coupling between the top and bottom AMBs of a FES system with a vertical rotor. The study presented simulation results that indicated that MPC was effective in reducing the effort needed to ensure robustness in the presence of disturbances and model uncertainties. A study conducted by Nguyen et. al [16, 17] implemented an MPC controller on a FES system and found that MPC was able to control the FES system effectively for quick acceleration and deceleration scenarios, that is, fast storing and releasing of energy. Current research tends to focus on nonlinear MPC approaches as described by the work of Bachle et. al [18].

In this paper, a linear state space model of an axially and radially AMB suspended flywheel is derived. This model is then used for the design of a linear MPC strategy. This control strategy is evaluated both in simulation and on an actual FES system. The results are compared to study the effectiveness of the control algorithm. The paper is organised as follows: The experimental setup of the FES system and the linear state space model derivation are discussed in Section 2. Section 3 introduces the linear MPC and the optimisation algorithm. Section 4 presents the simulation and experimental results. Finally, conclusions are drawn in Section 5.

2. FLYWHEEL ENERGY STORAGE SYSTEM MODEL

2.1 Flywheel energy storage system overview

The system under consideration is a Flywheel Uninterrupted Power Supply (FlyUPS) and is shown in Fig. 1. It is designed to deliver 2 kW of electrical energy for 3 minutes during power dips. The FlyUPS is fully suspended, which means it has five Degrees Of Freedom (DOF) controlled by two radial AMBs, and one axial AMB. The motor/generator mechanism of the FlyUPS contains a high speed Permanent Magnet Synchronous Machine (PMSM). This PMSM is designed to rotate the flywheel to speeds of up to 30 000 r/min which enables the FlyUPS to mechanically store 527 kJ of energy [19, 20].

2.2 State space model

A similar approach to [21] has been followed in this paper for deriving a state space model of the rotor and stator of the system. The effects of the sensors, filters and power amplifiers are also included to give a total state space system model of the FlyUPS. As illustrated in Fig. 2 the model includes five DOF: The translations in the x -, y -

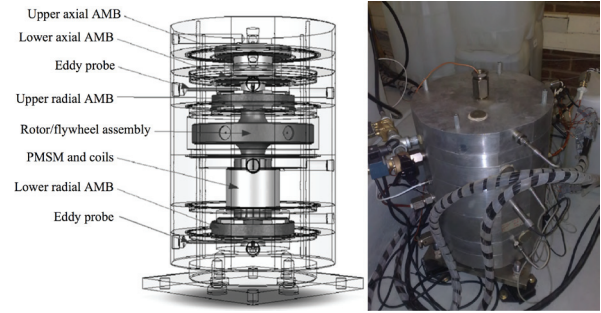


Figure 1: Experimental setup of the FlyUPS [19]

and z -directions, as well as the rotations about the x - and y -axes. The rotation about the z -axis is controlled by the PMSM. In order to develop a model for the rigid rotor,

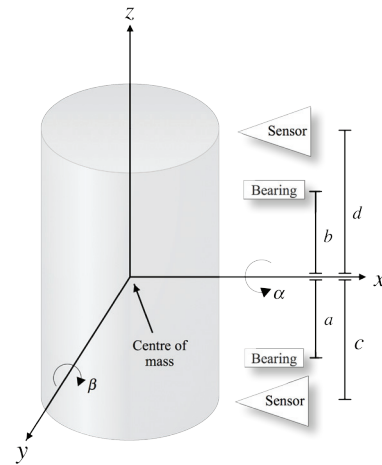


Figure 2: Rotor, bearing and sensor coordinate frame

a frame of reference (coordinate framework) first needs to be established. A rigid body can be represented by six coordinates: three displacement coordinates and three rotational coordinates. However, since the rotational speed is taken as constant and displacement in the axis of rotation is decoupled from the rest, the rotor can be represented by four coordinates only [22]. Hence, the coordinate framework is:

$$\mathbf{z} = [x, \beta, y, -\alpha]^T, \quad (1)$$

which represents the displacement (x, y) and inclination (β, α) about the centre of mass.

Once the coordinate framework is defined, the rotor and bearing dynamics are represented. The rotor dynamics of a simple gyroscopic beam can be represented by the Newton-Euler equations of motion [7]:

$$m\ddot{x} = f_x, \quad (2)$$

$$I_y\ddot{\beta} - I_z\Omega\dot{\alpha} = p_y, \quad (3)$$

$$m\ddot{y} = f_y, \quad (4)$$

$$-I_x\ddot{\alpha} - I_z\Omega\dot{\beta} = p_x. \quad (5)$$

The variables f_x and f_y are the forces acting on the centre of mass and p_y and p_x are the force couple moments. The rotor mass is represented by m , and Ω represents the constant angular velocity in rad/s about the z axis. I_x , I_y and I_z are the moments of inertia in the x , y and z directions respectively. The Newton-Euler equations above can be simplified by combining them with the selected coordinate framework in (1) to create the model

$$\mathbf{M}\ddot{\mathbf{z}} + \mathbf{G}\dot{\mathbf{z}} = \mathbf{f}, \quad (6)$$

with $\mathbf{f} = [f_x, p_y, f_y, p_x]$. \mathbf{M} is the mass matrix defined as

$$\mathbf{M} = \begin{bmatrix} m & 0 & 0 & 0 \\ 0 & I_y & 0 & 0 \\ 0 & 0 & m & 0 \\ 0 & 0 & 0 & I_x \end{bmatrix}, \quad (7)$$

and \mathbf{G} , the gyroscopic coupling matrix defined as

$$\mathbf{G} = \begin{bmatrix} 0 & 0 & 0 & 0 \\ 0 & 0 & 0 & 1 \\ 0 & 0 & 0 & 0 \\ 0 & -1 & 0 & 0 \end{bmatrix} I_z \Omega. \quad (8)$$

The actual system is current-controlled, necessitating coil current as input to the model [20]. A model with current as input and displacement as output is therefore required. However, since the actual position of the rotor is not available but only the measured position at the bearing sensor locations, it would be essential to transform or reference the above equations of motion to the bearing positions. The transformation from the centre of mass to the equivalent mass at the bearing locations, a and b , is done with the transformation matrix

$$\mathbf{T}_B = \frac{1}{b-a} \begin{bmatrix} b & -a & 0 & 0 \\ -1 & 1 & 0 & 0 \\ 0 & 0 & b & -a \\ 0 & 0 & -1 & 1 \end{bmatrix}. \quad (9)$$

The coordinate framework in (1) becomes

$$\mathbf{z} = \mathbf{T}_B \mathbf{z}_B = \mathbf{T}_B \begin{bmatrix} x_a \\ x_b \\ y_a \\ y_b \end{bmatrix}, \quad (10)$$

and the mass, gyroscopic and force matrices become

$$\mathbf{M}_B = \mathbf{T}_B^T \mathbf{M} \mathbf{T}_B, \quad (11)$$

$$\mathbf{G}_B = \mathbf{T}_B^T \mathbf{G} \mathbf{T}_B, \quad (12)$$

and

$$\mathbf{f}_B = \begin{bmatrix} f_{ax} \\ f_{bx} \\ f_{ay} \\ f_{by} \end{bmatrix}. \quad (13)$$

Finally the equation of motion can be written as

$$\mathbf{M}_B \ddot{\mathbf{z}}_B + \mathbf{G}_B \dot{\mathbf{z}}_B = \mathbf{f}_B. \quad (14)$$

The forces of the AMBs acting on the rotor are derived from a simple AMB model. The AMB plant constitutes a stator, coils and rotor as shown in Fig. 3. The position of the rotor is measured by two perpendicularly arranged position-sensors and subtracted from the reference position signal applied as the system input. The resulting error in position is converted by a compensator into current references, which in turn are realised by power amplifiers. In the AMB plant these currents exert electromagnetic forces on the rotor to restore the rotor position. Active

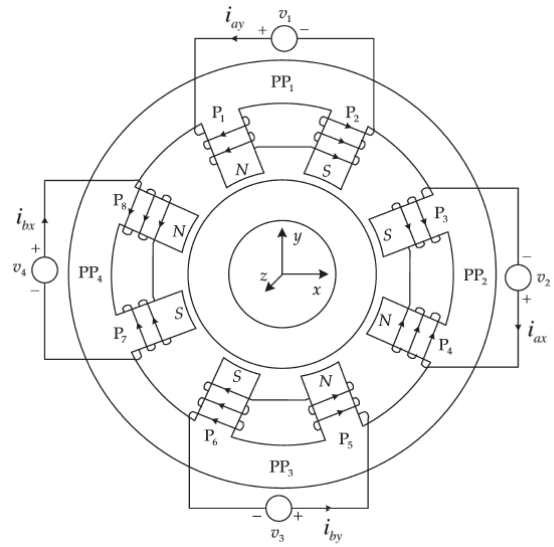


Figure 3: Stator of an 8-pole heteropolar AMB [23]

magnetic suspension (for a single magnet 1-DOF AMB) entails that an attractive magnetic force be exerted by an electromagnet that will counteract the gravitational force exerted by the earth. The attractive electromagnetic force exerted by a current-carrying coil on a ferromagnetic material is also known as a reluctance force [7]. This force is derived from the energy stored in the magnetic field. Any small change in the volume of the airgap would result in an increase in the energy stored in the field. This increase in energy must be supplied by an external force. If only the coils of the pole pair 1 (PP1) in Fig. 3 are allowed to carry a current and electromagnetic cross-coupling is ignored, the resulting force exerted in the y direction can be approximated by

$$f_m = \mu_0 \left(\frac{Ni}{l_c/\mu_r + 2x_g} \right)^2 A \cos(\theta) \quad (15)$$

with the symbols as described in Table 1.

The force equation for a 1-DOF AMB given in (15) shows the relationship between the applied current in the coil, the position of the shaft within the airgap and the

electromagnetic force exerted on the rotor by the stator pole. Clearly, the force is proportional to the square of the current as well as inversely proportional to the square of the airgap between the stator and the rotor.

Table 1: Symbol description of AMB force equation

Symbol	Description
l_c	length of the magnetic path (excluding the airgap)
μ_0	permeability of free space
μ_r	relative permeability of the AMB stator
x_g	size of the airgap between the stator and rotor
N	number of turns per coil
i	current in the coils
A	pole-face area
θ	angle between the vertical axis and the normal line to the pole face

This equation disregards the effects of fringing and leakage of magnetic flux and is only valid under the following assumptions [7]:

- permeability of the iron is constant;
- only small variations in the airgap are allowed; and
- uniform flux in the airgap (i.e. a homogeneous field).

Even when the effects of magnetic saturation and hysteresis have been disregarded, AMBs are still nonlinear devices, as can be seen from (15). In order to take advantage of the existing body of knowledge of linear systems, most AMB designers opt for linearising the AMB around a setpoint and controlling it as if it were a linear system. The range over which a linear approximation is valid, can be increased by driving opposing electromagnets in the AMB stator with mirror images of the same current signal. This is known as differential driving mode and is exhibited in Fig. 4 [7]. The schematic diagram in Fig. 4

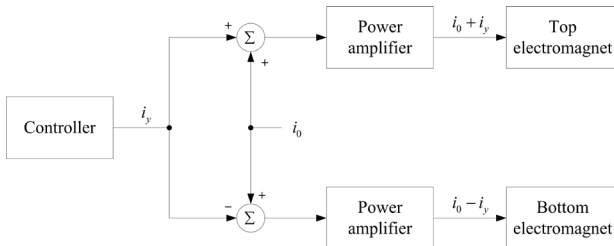


Figure 4: Schematic diagram of differential driving mode

only illustrates differential driving mode for the top and bottom electromagnets of the AMB in Fig. 3, but the same principle also holds for the other two electromagnets.

The output of the controller is a current reference signal which is added to and subtracted from a bias current level. The bias current is typically chosen such that the AMB is operated in the centre of the linear region of the magnetic material's hysteresis curve. The end result is that the nett force exerted by the top and bottom electromagnets is symmetrical about some bias force level. In the absence of gravity, the net electromagnetic force applied to the point mass is consequently given by:

$$f_m = k \left[\frac{(i_0 + i_y)^2}{(x_g)^2} - \frac{(i_0 - i_y)^2}{(x_g)^2} \right] \quad (16)$$

where the constants μ_0 , N , A and $\cos(\theta)$ have been subsumed into the constant k .

After linearising (16) for small position deviations (δ_y) around some bias position (y_0), the force exerted by an AMB in the vertical degree of freedom can be expressed as follows:

$$f_m = k_i i_y + k_s \delta_y \quad (17)$$

where the current- and position stiffness constants are respectively given by [20]:

$$k_i = 2 \frac{\mu_0 N^2 i_0 A}{y_0^2} \cos(\theta), \quad (18)$$

and

$$k_s = -2 \frac{\mu_0 N^2 i_0 A}{y_0^3} \cos(\theta). \quad (19)$$

According to (17) the bearing forces are dependent on current and displacement. These linearised forces are now introduced into the equation of motion (14) and result in

$$\mathbf{M}_B \ddot{\mathbf{z}}_B + \mathbf{G}_B \dot{\mathbf{z}}_B = \mathbf{K}_i \mathbf{i}_B + \mathbf{K}_s \mathbf{z}_B. \quad (20)$$

The displacement-force constants, \mathbf{K}_s and current-force constants, \mathbf{K}_i of the radial bearings are simply diagonal matrices of the previously mentioned, k_s and k_i constants:

$$\mathbf{K}_s = \begin{bmatrix} k_{s_{ax}} & 0 & 0 & 0 \\ 0 & k_{s_{bx}} & 0 & 0 \\ 0 & 0 & k_{s_{ay}} & 0 \\ 0 & 0 & 0 & k_{s_{by}} \end{bmatrix}, \quad (21)$$

and

$$\mathbf{K}_i = \begin{bmatrix} k_{i_{ax}} & 0 & 0 & 0 \\ 0 & k_{i_{bx}} & 0 & 0 \\ 0 & 0 & k_{i_{ay}} & 0 \\ 0 & 0 & 0 & k_{i_{by}} \end{bmatrix}. \quad (22)$$

The current-force and displacement-force values in the x and y directions at a and b are identical, i.e. $k_{s_{ax}} = k_{s_{ay}}$, and $k_{i_{bx}} = k_{i_{by}}$. The current vector is given by

$$\mathbf{i}_B = [i_{ax} \quad i_{bx} \quad i_{ay} \quad i_{by}]^T. \quad (23)$$

By rearranging (20) and setting $\mathbf{i}_B = \mathbf{u}$ the following equation is obtained

$$\ddot{\mathbf{z}}_B = -\mathbf{M}_B^{-1} \mathbf{G}_B \dot{\mathbf{z}}_B + \mathbf{M}_B^{-1} \mathbf{K}_s \mathbf{z}_B + \mathbf{M}_B^{-1} \mathbf{K}_i \mathbf{u}. \quad (24)$$

This gives the standard state-space formulation of the radial AMB system at the bearing coordinates as

$$\begin{aligned}\dot{\mathbf{x}}_B &= \mathbf{A}_B \mathbf{x}_B + \mathbf{B}_B \mathbf{u} \\ \mathbf{y}_B &= \mathbf{C}_B \mathbf{x}_B\end{aligned}\quad (25)$$

with

$$\mathbf{x}_B = \begin{bmatrix} \mathbf{z}_B \\ \dot{\mathbf{z}}_B \end{bmatrix}, \mathbf{A}_B = \begin{bmatrix} \mathbf{0} & \mathbf{I} \\ \mathbf{M}_B^{-1} \mathbf{K}_s & -\mathbf{M}_B^{-1} \mathbf{G}_B \end{bmatrix},$$

$$\mathbf{B}_B = \begin{bmatrix} \mathbf{0} \\ \mathbf{M}_B^{-1} \mathbf{K}_i \end{bmatrix}, \mathbf{C} = [\mathbf{I} \quad \mathbf{I}].$$

Next the transformation to sensor coordinates is done. The bearing coordinate state-space system in (25) is referenced to the sensor coordinate system by transforming the state matrices \mathbf{A}_B and \mathbf{B}_B to

$$\begin{aligned}\mathbf{A}_s &= \mathbf{T}_s \mathbf{A}_B \mathbf{T}_s^{-1}, \\ \mathbf{B}_s &= \mathbf{T}_s \mathbf{B}_B\end{aligned}\quad (26)$$

with

$$\mathbf{T}_s = \begin{bmatrix} \mathbf{S}_s \mathbf{T}_B & \mathbf{0} \\ \mathbf{0} & \mathbf{S}_s \mathbf{T}_B \end{bmatrix}, \quad (27)$$

and

$$\mathbf{S}_s = \begin{bmatrix} 1 & c & 0 & 0 \\ 1 & d & 0 & 0 \\ 0 & 0 & 1 & c \\ 0 & 0 & 1 & d \end{bmatrix}. \quad (28)$$

This results in the final state-space model

$$\begin{aligned}\dot{\mathbf{x}}_s &= \mathbf{A}_s \mathbf{x}_s + \mathbf{B}_s \mathbf{u} \\ \mathbf{y}_s &= \mathbf{C}_s \mathbf{x}_s\end{aligned}\quad (29)$$

with

$$\mathbf{x}_s = [x_c \quad x_d \quad y_c \quad y_d \quad \dot{x}_c \quad \dot{x}_d \quad \dot{y}_c \quad \dot{y}_d]^T. \quad (30)$$

The rotational speed of the rotor is taken into account in this model, and it can be seen from (20), that there is a coupling between the moment in the x plane and the moment in the y plane. As a consequence, this radial AMB model is a fully coupled system with four current inputs and eight outputs in terms of displacements and velocities respectively.

In addition to suspending the rotor horizontally, the FlyUPS system is required to lift and suspend the flywheel vertically. Consequently, the addition of an axial thrust bearing is required. The axial AMB is situated at the top of the FlyUPS rotor, and will use the thrust disc to exert the required lifting force. The axial AMB is taken as a simple 1-DOF point mass system, since axial rotor movement is assumed decoupled from the rotational movement due to rigid simple body motion, hence not influencing the centre of mass of the radial AMBs. There is no need to transform the axial model to bearing or sensor coordinates, as it represents vertical movement of a point mass system only.

The force acting on the axial AMB is calculated in a

similar manner as to (16), with the current-force and displacement-force values calculated similarly to (17), but with values for the axial AMB:

$$f(i_z, x_z) = k_{iz} i_z + k_{sz} x_z = m \ddot{z}. \quad (31)$$

The state space model for the axial AMB is given by

$$\begin{aligned}\dot{\mathbf{x}}_z &= \mathbf{A}_z \mathbf{x}_z + \mathbf{B}_z \mathbf{u}_z \\ \mathbf{y}_z &= \mathbf{C}_z \mathbf{x}_z\end{aligned}\quad (32)$$

with

$$\mathbf{x}_z = \begin{bmatrix} z \\ \dot{z} \end{bmatrix}, \mathbf{u}_z = [i_z], \mathbf{A}_z = \begin{bmatrix} 0 & 1 \\ \frac{k_{sz}}{m} & 0 \end{bmatrix},$$

$$\mathbf{B}_z = \begin{bmatrix} 0 \\ \frac{k_{iz}}{m} \end{bmatrix}, \mathbf{C}_z = [1 \quad 1].$$

The model for the axial AMB is simply appended to the model of the radial AMBs, as illustrated in Fig. 5 and the parameter values are. The sensors are modelled as five

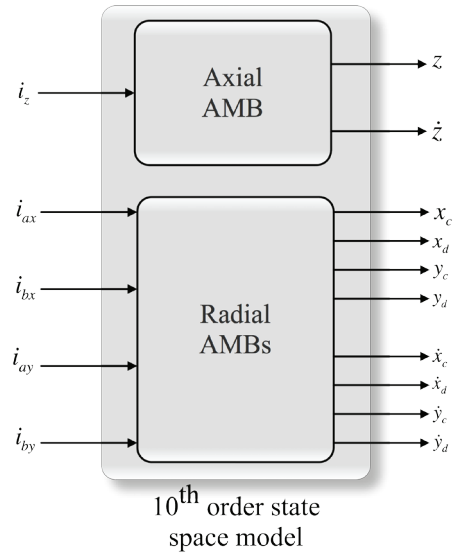


Figure 5: System state space model of FlyUPS

cascaded second order low-pass transfer functions with bandwidths of 10 kHz, and connected to the outputs of the AMB model [22]:

$$T_{sens}(s) = \frac{\omega_s^2}{s^2 + 2\zeta\omega_s s + \omega_s^2}, \quad (33)$$

with damping $\zeta = 0.707$ and bandwidth $\omega_s = 2 \cdot \pi \cdot 10 \times 10^3$ rad/s.

The power amplifier (PA) model consists of a closed loop PI controlled system with a bandwidth of 2.5 kHz as shown in Fig. 6. The closed loop transfer function of the PA is

given by

$$T_{PA}(s) = \frac{i_{out}(s)}{i_{ref}(s)} = \frac{2V_{bus}(K_i + K_p s)}{Ls^2 + (2K_p V_{bus} + R)s + 2K_i V_{bus}}, \quad (34)$$

where $V_{bus} = 51$ V is the bus voltage, $R = 0.152$ Ω is

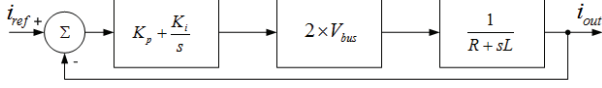


Figure 6: PA small signal closed-loop system

the coil resistance, $L = 6.494$ mH is the nominal coil inductance, $K_p = 1$ is the proportional constant and $K_i = 0.1$ is the integral constant [20]. The cascaded PA model is connected to the input of the AMB model.

3. MODEL PREDICTIVE CONTROL DESIGN

A conceptual diagram of a model predictive control system is shown in Fig. 7. A plant model is used to predict future values of the output variables. The differences between the reference signals and predicted outputs, serve as the input to an optimisation algorithm. At each sampling instant the control law uses the predicted information to generate the optimal inputs to the plant. Linear inequality constraints on the input and output variables, such as upper and lower limits, may be included in the calculation. The objective of the MPC control scheme is to determine a sequence of control moves (changes in the input variables) so that the predicted response moves to the set point in an optimal manner.

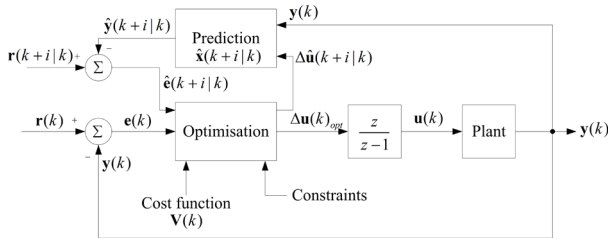


Figure 7: Conceptual diagram of MPC

Let the 5-DOF state space model be represented in a linearised, discrete-time, state space form

$$\begin{aligned} \mathbf{x}(k+1) &= \mathbf{A}\mathbf{x}(k) + \mathbf{B}\mathbf{u}(k), \\ \mathbf{y}(k) &= \mathbf{C}\mathbf{x}(k), \end{aligned} \quad (35)$$

where \mathbf{x} is an n -dimensional state vector, \mathbf{u} is an ℓ -dimensional input vector and \mathbf{y} is an m -dimensional output vector.

It is assumed that not all the state variables can be measured, and are therefore estimated/predicted. The following notation will be used to denote future values for

the variables $\mathbf{u}, \mathbf{x}, \mathbf{y}$ at time $k+i$, as assumed at time instant k :

$$\begin{aligned} \hat{\mathbf{u}}(k+i|k), \\ \hat{\mathbf{x}}(k+i|k), \\ \hat{\mathbf{y}}(k+i|k). \end{aligned}$$

The cost function $\mathbf{V}(k)$ penalises deviations of the predicted controlled outputs, $\hat{\mathbf{y}}(k+i|k)$, from the vector reference trajectory $\mathbf{r}(k+i|k)$. The cost function is defined as

$$\begin{aligned} \mathbf{V}(k) &= \sum_{i=H_w}^{H_p} \|\hat{\mathbf{y}}(k+i|k) - \mathbf{r}(k+i|k)\|_{\mathbf{Q}(i)}^2 \\ &\quad - \sum_{i=0}^{H_u-1} \|\Delta\hat{\mathbf{u}}(k+i|k)\|_{\mathbf{R}(i)}^2. \end{aligned} \quad (36)$$

H_p is the prediction horizon and H_u is the control horizon. It may not necessarily penalise the deviations of \mathbf{y} from \mathbf{r} immediately (if $H_w > 1$), since there may be some delay between applying the input and seeing the effect. It will be assumed that $H_u \leq H_p$, and that $\Delta\hat{\mathbf{u}}(k+i|k) = 0$. $\mathbf{Q}(i) \geq 0$ and $\mathbf{R}(i) \geq 0$ are weight matrices.

It will be assumed that $H_u \leq H_p$, and that $\Delta\hat{\mathbf{u}}(k+i|k) = 0$ for $i \geq H_u$. That means

$$\mathbf{u}(k+i|k) = \mathbf{u}(k+i+H_u|k) \text{ for all } i \geq H_u. \quad (37)$$

This cost function also implies that the predicted error vector $\hat{\mathbf{e}}(k+i|k) = \hat{\mathbf{y}}(k+i|k) - \mathbf{r}(k+i|k)$ is penalised at every point in the prediction horizon, in the range $H_w \leq i \leq H_p$.

The states of the system are predicted by iterating the state space model as follows:

$$\begin{aligned} \hat{\mathbf{x}}(k+1|k) &= \mathbf{A}\hat{\mathbf{x}}(k|k) + \mathbf{B}\hat{\mathbf{u}}(k|k) \\ \hat{\mathbf{x}}(k+2|k) &= \mathbf{A}\hat{\mathbf{x}}(k+1|k) + \mathbf{B}\hat{\mathbf{u}}(k+1|k) \\ &= \mathbf{A}^2\hat{\mathbf{x}}(k|k) + \mathbf{A}\mathbf{B}\hat{\mathbf{u}}(k|k) + \mathbf{B}\hat{\mathbf{u}}(k+1|k) \\ &\vdots \\ \hat{\mathbf{x}}(k+H_p|k) &= \mathbf{A}\hat{\mathbf{x}}(k+H_p-1|k) + \mathbf{B}\hat{\mathbf{u}}(k+H_p-1|k) \\ &= \mathbf{A}^{H_p}\hat{\mathbf{x}}(k|k) + \mathbf{A}^{H_p-1}\mathbf{B}\hat{\mathbf{u}}(k|k) + \dots \\ &\quad + \mathbf{B}\hat{\mathbf{u}}(k+H_p-1|k) \end{aligned} \quad (38)$$

The predicted input sequence is given by

$$\begin{aligned} \hat{\mathbf{u}}(k|k) &= \Delta\hat{\mathbf{u}}(k|k) + \mathbf{u}(k-1) \\ \hat{\mathbf{u}}(k+1|k) &= \Delta\hat{\mathbf{u}}(k+1|k) + \Delta\hat{\mathbf{u}}(k|k) + \mathbf{u}(k-1) \\ &\vdots \\ \hat{\mathbf{u}}(k+H_u-1|k) &= \Delta\hat{\mathbf{u}}(k+H_u-1|k) + \dots \\ &\quad + \Delta\hat{\mathbf{u}}(k|k) + \mathbf{u}(k-1) \end{aligned} \quad (39)$$

Substituting (39) into (38) results in the predicted state

equation

$$\mathbf{X}(k) = \Omega \mathbf{x}(k) + \Gamma \mathbf{u}(k-1) + \Phi \Delta \mathbf{U}(k) \quad (40)$$

where

$$\mathbf{X}(k) = \begin{bmatrix} \hat{\mathbf{x}}(k+1|k) \\ \vdots \\ \hat{\mathbf{x}}(k+H_p|k) \end{bmatrix}, \quad (41)$$

and

$$\Delta \mathbf{U}(k) = \begin{bmatrix} \Delta \hat{\mathbf{u}}(k|k) \\ \vdots \\ \Delta \hat{\mathbf{u}}(k+H_u-1|k) \end{bmatrix}, \quad (42)$$

for suitable matrices Ω , Γ and Φ .

The prediction of the output equation is obtained as

$$\begin{aligned} \hat{\mathbf{y}}(k+H_w|k) &= \mathbf{C} \hat{\mathbf{x}}(k+H_w|k) \\ \hat{\mathbf{y}}(k+H_w+1|k) &= \mathbf{C} \hat{\mathbf{x}}(k+H_w+1|k) \\ &\vdots \\ \hat{\mathbf{y}}(k+H_p|k) &= \mathbf{C} \hat{\mathbf{x}}(k+H_p|k) \end{aligned} \quad (43)$$

By substituting (39) and (38) into (43) the following compact representation of the output equation is obtained

$$\mathbf{Y}(k) = \Psi \mathbf{x}(k) + \Upsilon \mathbf{u}(k-1) + \Theta \Delta \mathbf{U}(k), \quad (44)$$

where

$$\mathbf{Y}(k) = \begin{bmatrix} \hat{\mathbf{y}}(k+H_w|k) \\ \vdots \\ \hat{\mathbf{y}}(k+H_p|k) \end{bmatrix}, \quad (45)$$

for suitable matrices Ψ , Υ and Θ .

The tracking error may then be defined as

$$\mathbf{E}(k) = \mathbf{T}(k) - \Psi \mathbf{x}(k) - \Upsilon \mathbf{u}(k-1) \quad (46)$$

where

$$\mathbf{T}(k) = \begin{bmatrix} \hat{\mathbf{r}}(k+H_w|k) \\ \vdots \\ \hat{\mathbf{r}}(k+H_p|k) \end{bmatrix}, \quad (47)$$

is the vector containing the reference signals.

The cost function may then be rewritten as follows

$$\mathbf{V}(k) = \|\mathbf{Y}(k) - \mathbf{T}(k)\|_{\bar{\mathbf{Q}}}^2 + \|\Delta \mathbf{U}(k)\|_{\bar{\mathbf{R}}}^2 \quad (48)$$

where

$$\bar{\mathbf{Q}} = \begin{bmatrix} \mathbf{Q}(H_w) & 0 & \cdots & 0 \\ 0 & \mathbf{Q}(H_w+1) & \cdots & 0 \\ \vdots & \vdots & \ddots & \vdots \\ 0 & 0 & \cdots & \mathbf{Q}(H_p) \end{bmatrix} \quad (49)$$

and

$$\bar{\mathbf{R}} = \begin{bmatrix} \mathbf{R}(0) & 0 & \cdots & 0 \\ 0 & \mathbf{R}(1) & \cdots & 0 \\ \vdots & \vdots & \ddots & \vdots \\ 0 & 0 & \cdots & \mathbf{R}(H_u-1) \end{bmatrix} \quad (50)$$

Equation (48) may be written in its expanded form as

$$\begin{aligned} \mathbf{V}(k) &= \mathbf{E}(k)^T \bar{\mathbf{Q}} \mathbf{E}(k) - 2 \Delta \mathbf{U}(k)^T \Phi^T \bar{\mathbf{Q}} \mathbf{E}(k) \\ &\quad + \Delta \mathbf{U}(k)^T [\Theta^T \bar{\mathbf{Q}} \Theta + \bar{\mathbf{R}}] \Delta \mathbf{U}(k). \end{aligned} \quad (51)$$

This equation may also be written in the form

$$\mathbf{V}(k) = \text{const} - \Delta \mathbf{U}(k)^T \mathbf{G} + \Delta \mathbf{U}(k)^T \mathbf{H} \Delta \mathbf{U}(k), \quad (52)$$

where

$$\mathbf{G} = 2 \Theta^T \bar{\mathbf{Q}} \mathbf{E}(k) \quad (53)$$

and

$$\mathbf{H} = \Theta^T \bar{\mathbf{Q}} \Theta + \bar{\mathbf{R}} \quad (54)$$

and neither \mathbf{G} nor \mathbf{H} depends on $\Delta \mathbf{U}(k)$. In order to find the optimal $\mathbf{U}(k)$, the gradient of $\mathbf{V}(k)$ is set to zero

$$\nabla_{\Delta \mathbf{U}(k)} = -\mathbf{G} + 2\mathbf{H}\Delta \mathbf{U}(k) \quad (55)$$

implying that the optimal set of future input moves is

$$\Delta \mathbf{U}(k)_{opt} = \frac{1}{2} \mathbf{H}^{-1} \mathbf{G}. \quad (56)$$

It should be remembered that due to the use of the concept of a receding horizon, only the first part of the solution corresponding to the first step is used. Therefore, if the plant has ℓ inputs, then only the first ℓ rows of the vector $\Delta \mathbf{U}(k)_{opt}$ are used. This may be represented as follows

$$\Delta \mathbf{u}(k)_{opt} = [\mathbf{I}_\ell, \mathbf{0}_\ell, \cdots, \mathbf{0}_\ell] \Delta \mathbf{U}(k)_{opt}, \quad (57)$$

where \mathbf{I}_ℓ is the $\ell \times \ell$ identity matrix, and $\mathbf{0}_\ell$ is the $\ell \times \ell$ zero matrix.

4. RESULTS

The MPC control was implemented on a hardware platform as depicted in Fig. 8. The code for the MPC controller was implemented in Simulink[®]. Using the Real-Time Workshop[®], the Simulink[®] code is converted to C code and compiled as an executable file. The executable file is then linked and embedded on a dSPACE[®] real-time control target board.

The user can monitor the FlyUPS with a host computer through dSPACE[®] ControlDesk[®] software. ControlDesk[®] is used for displaying the system status in real-time. From here the PMSM drive can be activated and changes to the reference signals can be made.

4.1 Memory usage and cycle time

Memory usage of the controller is described in terms of the size of the executable file that needs to be embedded

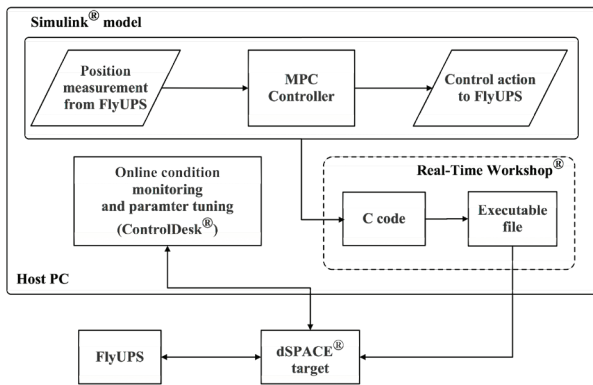


Figure 8: Implementation method of MPC on FlyUPS

on the dSPACE[®] hardware. The full five DOF MPC controller for the FlyUPS uses 12.7 MB of memory, which is well below the limit of 16 MB maximum storage of the dSPACE[®] target.

The execution time of the controller indicates the period of time it takes to implement the control strategy during one control cycle. This includes reading the measured outputs of the system, calculating the optimal control signal, and implementing the optimal control action. In order to determine the execution time of the MPC controller the dSPACE[®] Profiler[®] is used. The profiler logs the period of time that passes from the start of the control cycle until the control action is implemented.

Various factors influence the execution time of the FlyUPS control system. These factors include the order of the model from which the controller is derived, the use of constraints in the design, and the lengths of H_p and H_u . This is expected as these factors increase the complexity and number of operations that are performed during each cycle.

It was determined experimentally that the largest sampling period for the FlyUPS control system to maintain stability is 200 μ s, corresponding to a sampling frequency of 5 kHz. For the unconstrained 5 DOF MIMO MPC control strategy, the execution time is 174 μ s. This unconstrained controller is derived from a reduced tenth order state space model. However, when constraints were included the controller became unstable due an execution time larger than 200 μ s. The effects of the prediction and control horizons were investigated by keeping one parameter fixed and varying the other parameter. It turned out that the optimal choice of these parameters adhering to the maximum execution time, was $H_p = 50$ and $H_u = 5$.

4.2 Sensitivity analysis

A comparison of the measured and simulated sensitivity functions for the axial AMB (Z), top radial AMB ($X1$) and bottom radial AMB ($X2$) at standstill are given in Figures 9, 10 and 11 respectively.

From Fig. 9 the peak measured sensitivities of the axial AMB are 4.15 dB at 44.21 Hz and 16.22 dB at 81.76 Hz corresponding to the first two rigid modes of the axial AMB. The peak of 16.22 dB places the axial AMB of the FlyUPS in class D of the ISO CD 14839-3 standard. This measured result reveals that the axial AMB of the FlyUPS is very sensitive to parameter changes from 82 Hz to 96.5 Hz. The simulated sensitivity function clearly does not predict this sensitivity. The simulation result indicates a single peak sensitivity of 4 dB at 160 Hz placing the axial AMB in zone A of the ISO CD 14839-3 standard. This difference indicates that the model of the axial AMB may not be accurate enough to meet the requirements of MPC.

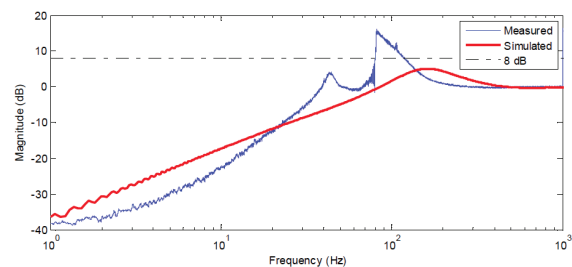


Figure 9: Sensitivity function of the axial AMB at standstill

Fig. 10 and Fig. 11 give the results for the sensitivity functions of the top and bottom radial AMBS respectively, at standstill. These results indicate a larger correlation between the simulated and measured results. However, it is also clear from these results that the actual system has some inherent dynamics that are not contained in the model and thus do not appear on the simulation results.

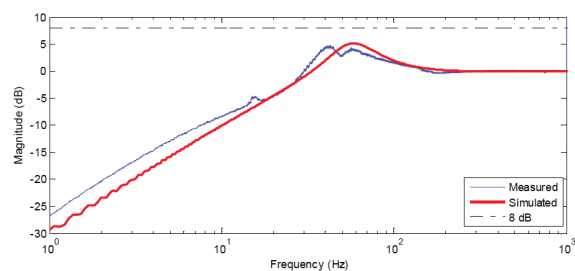


Figure 10: Sensitivity function of the top radial AMB at standstill

Fig. 10 shows three peak sensitivities of -4.82 dB, 4.728 dB and 4.14 dB at 15.38 Hz, 42.16 Hz and 57.63 Hz, respectively, in the measured sensitivity of $X1$ at standstill. This places the top radial AMBs within zone A of the ISO CD 14839-3 standard of AMBs. The simulated sensitivity expects a single peak of 5 dB at 58 Hz corresponding to zone A of the ISO CD 14839-3 standard.

At standstill, the measured sensitivity function of $X2$ given in Fig. 11 shows peaks in the sensitivity of 3.18 dB and 4.13 dB, at 15.13 Hz and 34.93 Hz, respectively. This

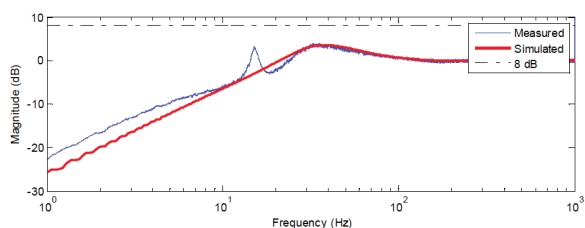


Figure 11: Sensitivity function of the bottom radial AMB at standstill

places the bottom radial AMBs within the class A of the ISO CD 14839-3 standard on AMBs. The simulated sensitivity of X2 indicates a single peak of 4.1 dB at 35 Hz corresponding to zone A of the ISO CD 14839-3 standard as well.

Despite the low sensitivities of the radial AMBs to parameter changes, the system is classified according to the worst case measured sensitivity. This means that the FlyUPS falls within class D of the ISO CD 14839-3 standard due to the peak sensitivity of the axial AMB. For MPC the shape of the sensitivity function is expected as the controller is derived from the model of the FlyUPS at standstill. This means that low sensitivities are expected at low frequencies, with the gain of the sensitivity function increasing as the operating speed increases.

The sensitivity functions of Z, X1 and X2 only change marginally from operation at standstill to an operating speed of 500 r/min in both simulation and implementation. These results are given in Fig. 12, Fig. 13 and Fig. 14 for Z, X1 and X2, respectively. The major change that is noted in the results is the increase in the frequency components corresponding to integer multiples-of-two harmonics of the operating speed, indicating the presence of an unbalance [7]. These harmonics do not appear to have a large effect on the sensitivity of the axial AMB. However, in the case of the radial AMBs the sensitivity at these harmonic frequencies is driven into zone D of the ISO CD 14839-3 standard for AMBs.

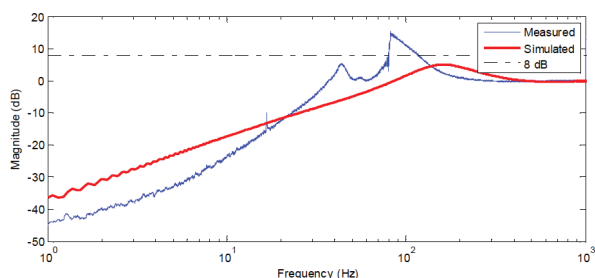


Figure 12: Sensitivity function of the axial AMB at 500 r/min

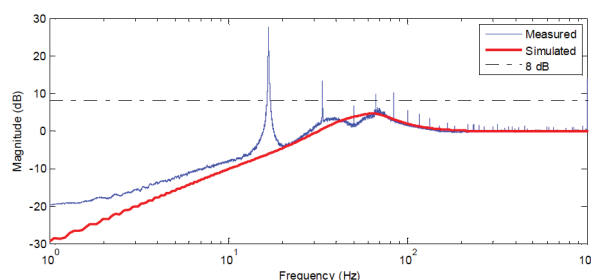


Figure 13: Sensitivity function of the top radial AMBs at 500 r/min

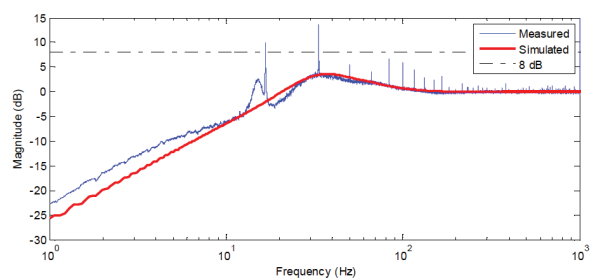


Figure 14: Sensitivity function of the bottom radial AMBs at 500 r/min

4.3 MPC operating range

The operating range is defined as the amount by which the operating speed can be adjusted about the design speed of the MPC controller before the system response becomes unstable. This is done by implementing an MPC controller derived for the model of the FlyUPS at standstill and increasing the operating speed until the maximum operating speed is attained where the radius of the orbital pattern about the origin reaches $120 \mu\text{m}$.

An increase in the operating speed introduces a visible change in the performance of the MPC controller in simulation and implementation where the radius of the orbital pattern increases nearly exponentially as the operating speed is increased. In the case of the simulation, the maximum operating speed reached is 2440 r/min for an orbital radius of $120 \mu\text{m}$ in X1. In the experimental setup the orbital radius of $120 \mu\text{m}$ in X1 is already reached at 1500 r/min. Any further increase in the operating speed of the implementation causes the open-loop PMSM control to lose synchronism with the rotor. This point along with the restriction in terms of cycle time resulted in the choice of the 500 r/min operating speed for the test results.

5. CONCLUSIONS

In order to evaluate the implementation of MPC on the FlyUPS the MPC controller was firstly validated by comparing the performance of the implementation to the simulated performance. This comparison showed that the performance of the practical implementation correlated to

the performance expected in simulation with regard to the sensitivity analysis.

However, at an operating speed of 500 r/min an unbalance disturbance is noted in the response of the radial AMBs. This unbalance is seen as the sinusoidal disturbance in the position output of the radial AMBs and can be identified by the integer multiples-of-two harmonic components in the frequency response that are introduced by the unbalance at the operating speed. From these results it is clear that the MPC controller is limited to the design parameters derived at standstill, which cannot implement enough stiffness in the AMBs to eliminate the unbalance. Some limitations regarding the operating range due to unmodelled dynamics, as well as long execution times due to the computational load have also been noticed.

In this paper it was shown that MPC is a viable control strategy for the FlyUPS, however some limitations of the current MPC strategy needs to be addressed to improve performance at higher operating speeds.

One of the main limiting factors is the optimisation algorithm of the MPC control strategy that utilises a model of the actual system. In this regard other types of models such as artificial neural networks or fuzzy models can be incorporated. These models are also able to update on-line as the operating point changes. This may be very beneficial in terms of the operating speed range.

For the optimisation algorithm various techniques have been proposed for the reduction of the computational load when calculating the optimal control action for a MIMO system. The most prominent technique involves convex optimisation algorithms that reduce the computational load by exploiting special patterns in the formulation of the objective function. This technique is common in applications involving quadratic programming problems such as the formulation of the MPC cost function when constraints are implemented on the output and the increment of the control signals. Alternatively the parameters that do not change during the plant operation can be identified and calculated offline to reduce the computational load. These parameters can then be implemented in a gain-scheduling algorithm during operation.

REFERENCES

- [1] A. Stodola, *Steam and Gas Turbines*. New York, USA: McGraw-Hill Book Company, Inc., 1927.
- [2] J. Bitterly, "Flywheel technology: past, present, and 21st century projections," *Aerospace and Electronic Systems Magazine, IEEE*, pp. 2312–2315, 1998.
- [3] D. Christopher and R. Beach, "Flywheel technology development program for aerospace applications," in *Proceedings of the IEEE 1997 National Aerospace and Electronics Conference*, 1997, pp. 602–608.
- [4] R. Hebner, J. Beno, and A. Walls, "Flywheel batteries come around again," *Spectrum, IEEE*, 2002.
- [5] H. Liu and J. Jiang, "Flywheel energy storage: An upswing technology for energy sustainability," *Energy and buildings*, vol. 39, pp. 599–604, 2007.
- [6] B. Bolund, H. Bernhoff, and M. Leijon, "Flywheel energy and power storage systems," *Renewable and Sustainable Energy Reviews*, vol. 11, no. 2, pp. 235–258, 2007.
- [7] G. Schweitzer, E. Maslen, and H. Bleuler, *Magnetic Bearings: Theory, Design, and Application to Rotating Machinery*. Springer, 2009.
- [8] J. C. Doyle and G. Stein, "Multivariable Feedback Design: Concepts for a Classical/Modern Synthesis," *IEEE Transactions on Automatic Control*, vol. 26, no. 1, pp. 4–16, 1981.
- [9] G. J. Balas, J. C. Doyle, K. Glover, A. Packard, and R. Smith, " μ -Analysis and Synthesis Toolbox For Use with MATLAB," Natick, 2001.
- [10] A. Lanzon and P. Tsiotras, "A Combined Application of H_∞ Loop Shaping and μ -Synthesis to Control High-Speed Flywheels," *IEEE Transactions on Automatic Control*, vol. 13, no. 5, pp. 766–777, 2005.
- [11] J. T. Sawicki, E. H. Maslen, and K. R. Bischof, "Modeling and Performance Evaluation of Machining Spindle with Active Magnetic Bearings," *Journal of Mechanical Science and Technology*, vol. 21, pp. 847–850, 2007.
- [12] S. Steyn, P. van Vuuren, and G. van Schoor, "Multivariable H_∞ Control for an Active Magnetic Bearing Flywheel System," *UKACC International Conference on CONTROL 2010*, pp. 1014–1019, 2010.
- [13] K. Nonami, W. He, and H. Nishimura, "Robust Control of Magnetic Levitation Systems by Means of H_∞ Control/ μ -Synthesis," *JSME International Journal*, vol. 37, no. 3, pp. 513–520, 1994.
- [14] C. Zhang and K. Tseng, "Model-based predictive control for a compact and efficient flywheel energy storage system with magnetically assisted bearings," in *35th Annual IEEE Power Electronics Specialists Conference*, Aachen, Germany, 2004, pp. 3573–3579.
- [15] K. Y. Zhu, Y. Xiao, and A. U. Rajendra, "Optimal control of the magnetic bearings for a flywheel energy storage system," *Mechatronics*, vol. 19, no. 8, pp. 1221–1235, 2009.
- [16] T. Nguyen and K. Tseng, "Model predictive control of a novel axial flux permanent magnet machine for flywheel energy storage system," in *IPEC, 2010 Conference Proceedings*, 2010, pp. 519 – 524.
- [17] —, "On the modeling and control of a novel flywheel energy storage system," in *Industrial Electronics (ISIE), 2010 IEEE International Symposium on*, 2010, pp. 1395–1401.

- [18] T. Bächle, S. Hentzelt, and K. Graichen, "Nonlinear model predictive control of a magnetic levitation system," *Control Engineering Practice*, vol. 21, no. 9, pp. 1250–1258, 2013.
- [19] J. Janse van Rensburg, "Development of a flywheel energy storage system - Uninterruptable power supply," Masters' Thesis, North-West University, Potchefstroom, 2007.
- [20] S. Myburgh, "The development of a fully suspended AMB system for a high-speed flywheel application," Masters' Thesis, North-West University, Potchefstroom, 2007.
- [21] S. Steyn, "Multivariable \mathcal{H}_∞ Control for an Active Magnetic Bearing Flywheel System," Masters' Thesis, North-West University, Potchefstroom, 2010.
- [22] B. Aeschlimann, "Control Aspects of High Precision Active Magnetic Bearings," PhD, 2002.
- [23] E. Ranft, "An improved model for self-sensing heteropolar active magnetic bearings," PhD thesis, North-West University, 2007.

APPENDIX A

Parameter values used in the state space model are given in the following Tables.

Table 1: Parameter values of the FlyUPS

Symbol	Description	Value	Unit
I_x	Moment of inertia in the x plane	0.11575	$\text{kg} \cdot \text{m}^2$
I_y	Moment of inertia in the y plane	0.11575	$\text{kg} \cdot \text{m}^2$
I_z	Moment of inertia in the z plane	0.10669	$\text{kg} \cdot \text{m}^2$
m	Mass of the rotor	17.65	kg
a	Bearing displacement	-160×10^{-3}	m
b	Bearing displacement	64.4×10^{-3}	m
c	Bearing displacement	-190×10^{-3}	m
d	Bearing displacement	95.4×10^{-3}	m

Table 2: Parameter values for the radial bearings

Symbol	Description	Value	Unit
k_i	Force-current constant	30	N/A
k_s	Force-displacement constant	-15000	N/m
μ_0	-	$4\pi \times 10^{-7}$	-
A	-	204.026×10^{-6}	m^2
N	-	80	-
i_0	-	2.5	A
y_0	-	500×10^{-6}	m
θ	-	22.5°	-

Table 3: Parameter values for the axial bearings

Symbol	Description	Value	Unit
k_{iz}	Force-current constant	54.9	N/A
k_{sz}	Force-displacement constant	-329693	N/m
μ_0	-	$4\pi \times 10^{-7}$	-
A	-	168.45×10^{-6}	m^2
N	-	104	-
i_0	-	3	A
z_0	-	500×10^{-6}	m
θ	-	0°	-